PAPER

Check for updates

Photoluminescence modal splitting *via* strong coupling in hybrid Au/WS₂/GaP nanoparticle-on-mirror cavities†

Merve Gülmüs,[a] Thomas Possmayer, [ID] [a] Benjamin Tilmann, [ID] [a] Paul Butler, [ID] [b,c]
Ian D. Sharp, [ID] [b,c] Leonardo de S. Menezes, [ID] [a,d] Stefan A. Maier [ID] [e,f] and
Luca Sortino [ID] *[a]

By integrating dielectric and metallic components, hybrid nanophotonic devices present promising opportunities for manipulating nanoscale light–matter interactions. Here, we investigate hybrid nanoparticle-on-mirror optical cavities, where semiconductor WS₂ monolayers are positioned between gallium phosphide (GaP) nanoantennas and a gold mirror, thereby establishing extreme confinement of optical fields. Prior to integration of the mirror, we observe an intermediate coupling regime from GaP nanoantennas covered with WS₂ monolayers. Upon introduction of the mirror, enhanced interactions lead to modal splitting in the exciton photoluminescence spectra, spatially localized within the dielectric-metallic gap. Using a coupled harmonic oscillator model, we extract an average Rabi splitting energy of 22.6 meV at room temperature, at the onset of the strong coupling regime. Moreover, the characteristics of polaritonic emission are revealed by the increasing Lorentzian linewidth and energy blueshift with increasing excitation power. Our findings highlight hybrid nanophotonic structures as novel platforms for controlling light–matter coupling with atomically thin materials.

Introduction

Nanoscale gaps focus light into sub-nm regions between closely spaced optically resonant surfaces,[1,2] providing atomic-scale interactions driving the emergence of quantum features in nanoscale electromagnetism,[3–5] and strong field confinement for efficient light–matter coupling and surface-enhanced spectroscopies.[6,7] Within this context, the exceptional optoelectronic properties of two-dimensional (2D) materials make them appealing for integration into nanophotonic gaps featur-

ᵃChair in Hybrid Nanosystems, Nanoinstitute Munich, Faculty of Physics, Ludwig-Maximilians-Universität München, 80539 Munich, Germany.
E-mail: luca.sortino@physik.uni-muenchen.de
ᵇWalter Schottky Institute, Technische Universität München, Am Coulombwall 4, 85748 Garching, Germany
ᶜPhysics Department, TUM School of Natural Sciences, Technische Universität München, Am Coulombwall 4, 85748 Garching, Germany
ᵈDepartamento de Física, Universidade Federal de Pernambuco, 50670-901 Recife, PE, Brazil
ᵉSchool of Physics and Astronomy, Monash University, Clayton, Victoria 3800, Australia
ᶠThe Blackett Laboratory, Department of Physics, Imperial College London, London, SW7 2BW, UK
†Electronic supplementary information (ESI) available. See DOI: https://doi.org/10.1039/d4nr03166k

ing extreme light confinement.[8,9] In particular, 2D semiconductors, such as transition metal dichalcogenides (TMDCs), are promising active materials for nanophotonic devices.[10–12] At the single layer limit, they offer stable excitonic resonances and can be deterministically manipulated for device fabrication.[13] 2D semiconductors placed between a reflective metallic mirror and a resonant plasmonic nanoparticle, in a so-called nanoparticle-on-mirror geometry, have served as the basis for numerous studies of strong light–matter coupling under ambient conditions,[14–18] nonlinear optics,[19,20] and for deterministic coupling of single photon sources.[21,22] While such structures represent a viable platform for achieving strong coupling, observation of photoluminescence (PL) emission from polaritonic states in plasmonic systems is hindered by low quantum efficiencies and the dissipative nature of plasmonic resonances. Thus, signatures of strongly coupled systems based on embedded 2D semiconductors have primarily been studied by means of scattering and non-linear optical processes.[23] Polaritonic PL emission has been reported from plasmonic nanoparticle-on-mirror cavities with embedded organic molecules at cryogenic temperatures[24] and PL signatures of strong coupling were observed for 2D semiconductors in tip-enhanced plasmonic nanogaps,[25] however, the detection of polaritonic luminescence signatures in particle-on-mirror geometries remains extremely challen-

ging owing to high optical losses, broad spectral overlap, spatial and temporal fluctuations in the local field environment and quenching mechanisms at metal–dielectric interfaces.[15,23,26] For this purpose, hybrid nanocavities combining Mie resonant dielectric nanoparticles with metallic mirrors offer a new approach to overcome the limitations of plasmonic systems, usually suffering from intrinsic ohmic losses.[27] The inclusion of a dielectric component helps to mitigate these losses, while providing greater flexibility in tuning the optical properties of the nanocavity through the careful selection of materials and their geometry. Although such optical cavities have been the subject of theoretical investigations,[28,29] experimental demonstrations have so far been restricted to the use of random dispersions of spherical dielectric nanoparticles[30–32] and evidence of polaritonic PL emission has only been partially observed.[33]

In this work, we investigated the interaction between top-down lithographically defined cylindrical gallium phosphide (GaP) dielectric nanoparticle-on-mirror cavities and excitons in a WS_2 TMDC monolayer. We first transfer the monolayer onto GaP nanoantenna arrays, observing strain signatures and PL emission enhancement, confirming an intermediate light–matter coupling regime in the scattering response. By introducing a reflective gold mirror, we enhance the light–matter coupling strength *via* extreme field confinement in the nanometer-sized gap. The effective coupling is observed as a modal splitting in the WS_2 PL emission spectra, spatially localized within the nanoscale gap cavity. We employ a coupled oscillator model (COM) to describe the coherent interaction between excitons and cavity modes and extract Rabi splitting energies in the range of 20–24 meV, placing the system at the onset of the strong coupling regime. Furthermore, the strain-dependent emission from the monolayer allows us to disentangle the roles of different excitonic states to the coupling, with spectral analysis revealing a prominent Lorentzian character of the polaritonic emission from the nanocavity. With increased optical excitation power, we observe a blueshift of the coupled exciton emission, further indicating non-linear polariton interactions. Our results hold promise for the development of hybrid nanophotonic structures, emphasizing the synergistic potential of combining dielectric and metallic nanocavities for enhanced light–matter interactions with 2D materials.

Results

The hybrid dielectric-on-mirror nanocavity (Fig. 1a) is composed of a Mie resonant GaP antenna and a gold mirror. An additional thin (3 nm) dielectric spacer of alumina (Al_2O_3) is grown on the gold surface using atomic layer deposition (ALD) to preserve the optical efficiency of the 2D semiconductor. By embedding a WS_2 monolayer within the gap, the enhanced interaction of excitons with the strongly confined field pushes the system towards the strong light–matter coupling regime *via* hybridization of the photon–exciton coupled system (Fig. 1b). By modelling a single photon and an exciton as coupled har-

monic oscillators, the interaction between light and matter can be described using the following Hamiltonian:[12]

$$H = \begin{pmatrix} \omega_{cav} - i\kappa & g \\ g & \omega_X - i\gamma \end{pmatrix} \quad (1)$$

where κ and γ are the decay rates of the cavity and exciton respectively, expressed as the full width half maximum, ω_{cav} and ω_X are the cavity and the exciton frequencies, and $g = \sum_i \sqrt{g_i}$ is the coupling strength defined by the superposition of all the excitons taking part in the strong coupling condition. The off-diagonal terms introduce the coupling strength between the two oscillators. When the coupling strength overcomes the dissipative losses ($|g| \gg |\gamma|, |\kappa|$), the system enters the strong coupling regime and two distinct eigenmodes, or dressed states, are created. These are known as the lower (LP) and upper (UP) polariton branches, separated by the Rabi energy (Ω_R), and exhibit mixed light–matter properties, with energies defined by:[12]

$$\omega_{LP,UP} = \frac{\omega_{cav} + \omega_X}{2} - i\frac{\kappa + \gamma}{2}$$
$$\pm \sqrt{\left(\frac{\omega_{cav} - \omega_X}{2} - i\frac{\kappa - \gamma}{2}\right)^2 + g^2} \quad (2)$$

with an associated energy splitting of $\Omega_R = \sqrt{[\omega_{cav} - \omega_X - i(\kappa - \gamma)]^2 + 4g^2}$. When the condition $|g| > \left|\frac{\kappa + \gamma}{4}\right|$ is satisfied, such that the splitting exceeds the combined spectral widths of both resonances, the coupled system overcomes the threshold needed to enter the strong coupling regime. We then define a normalized strong coupling condition threshold: $4g/(\kappa + \gamma) = 1$. When the coupling strength approaches this condition, and satisfies $4g/(\kappa + \gamma) > 0.5$, we define the intermediate light–matter coupling regime.[23,34]

Several key factors contribute to the realization of the strong coupling regime, most notably the need for strong electromagnetic field intensities ($\sim|E|^2$) in resonance with material emitters possessing strong transition dipole moments, all confined within a small effective modal volume. For this purpose, 2D TMDC semiconductors are especially versatile, with atomic scale thicknesses suitable for probing the confined optical fields in nanoparticle-on-mirror geometries.[35] WS_2 stands out due to its large exciton binding energies and oscillator strengths that arise from reduced dielectric screening and increased quantum confinement, as well as its transition to direct bandgap at the monolayer limit, which facilitates the coupling with light.[13] Additionally, single atomic TMDC layers can be deterministically manipulated and transferred on top of optically resonant dielectric nanostructures,[36,37] or integrated in vertical van der Waals heterostructures,[38] further extending the design opportunities for hybrid nanophotonic devices.

In this work, we first designed our nanoparticle-on-mirror cavities with finite-difference time-domain (FDTD) numerical simulations. Fig. 1c–e shows the results of the simulated electric field enhancement ($|E|/|E_0|)^2$ of both a single GaP nanoantenna
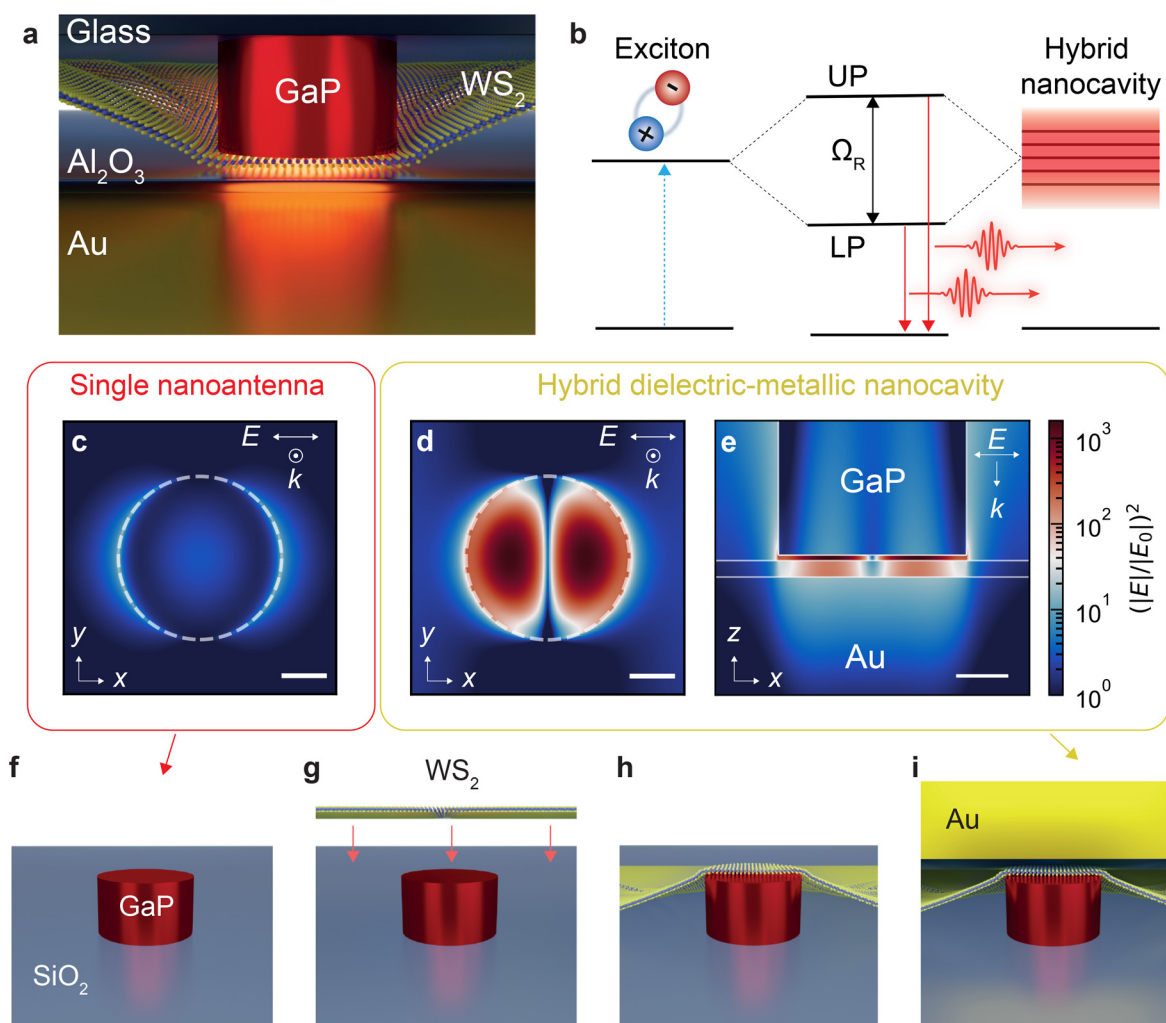
Fig. 1 (a) Illustration of the hybrid dielectric nanoparticle-on-mirror cavity. (b) Schematics of strong light–matter coupling between 2D excitons and cavity modes, with formation of the lower (LP) and upper (UP) polariton branches, where Ω_R is the Rabi energy splitting. (c) Numerically simulated electric field intensity $(|E|/|E_0|)^2$ scattered by a GaP nanoantenna (90 nm radius and 100 nm height) on a silica substrate. The field monitor is positioned at 0.5 nm above the top surface. (d) Simulated electric field intensity for the same nanoantenna in panel c, placed on a gold mirror, evaluated 0.5 nm above the top surface of the nanoantenna. (e) Simulated electric field intensity of the hybrid dielectric-on-mirror nanocavity collected along the x,z-plane. Scale bars in (c–e) are 50 nm. (f–i) Fabrication steps of the hybrid dielectric-on-mirror nanocavity. (f) Top-down fabrication of GaP nanoantennas on the silica substrate. (g) Exfoliation and alignment of a WS_2 monolayer above the nanoantenna. (h) Transfer of the WS_2 monolayer onto the nanoantenna. (i) Assembly of the hybrid nanocavity via placement of the gold mirror on top of the WS_2/GaP nanoantenna.

and the hybrid dielectric-metallic mirror nanocavity. The electric field intensity of the scattered radiation, $|E|^2$, is normalized to the intensity of the linearly polarized normal incidence plane wave, $|E_0|^2$, at a wavelength of 619 nm, which is resonant with WS_2 exciton emission. Fig. 1c presents the simulated intensity at the top surface of a single GaP nanoantenna with 90 nm radius and 100 nm height, showing a 10-fold increase of the scattered field intensity. This enhancement is particularly concentrated at the edges and is influenced by the geometry of the nanoantenna.[36] As expected, the addition of the gold mirror enhances the field intensity by a factor of 10^3 (Fig. 1d and e), owing to the extreme confinement within the 1 nm gap.

Considering the promising results predicted from simulation, we proceeded with fabrication of the hybrid nanocavity following

the steps shown in Fig. 1f–i (see also ESI note 1†). First, arrays of GaP nanoantennas (height of 100 nm and radius spanning from 85 nm to 135 nm) were fabricated on SiO_2 substrates with standard top-down lithography processes. We then mechanically exfoliated, aligned, and transferred WS_2 monolayers on top of the nanoantennas using an all-dry stamping method (Fig. 1g and h). To finalize the mirror component, a gold film was sputtered onto a fused silica substrate and a 3 nm thick Al_2O_3 dielectric spacer was deposited onto the gold film resulting in a surface roughness below 1 nm (see ESI note 1†). Finally, the hybrid nanocavity was completed by positioning the gold mirror, as shown in Fig. 1i, thereby creating the nanoscale gap.

Fig. 2a displays the experimental dark field scattering data from the fabricated GaP nanoantenna array, along with a com-
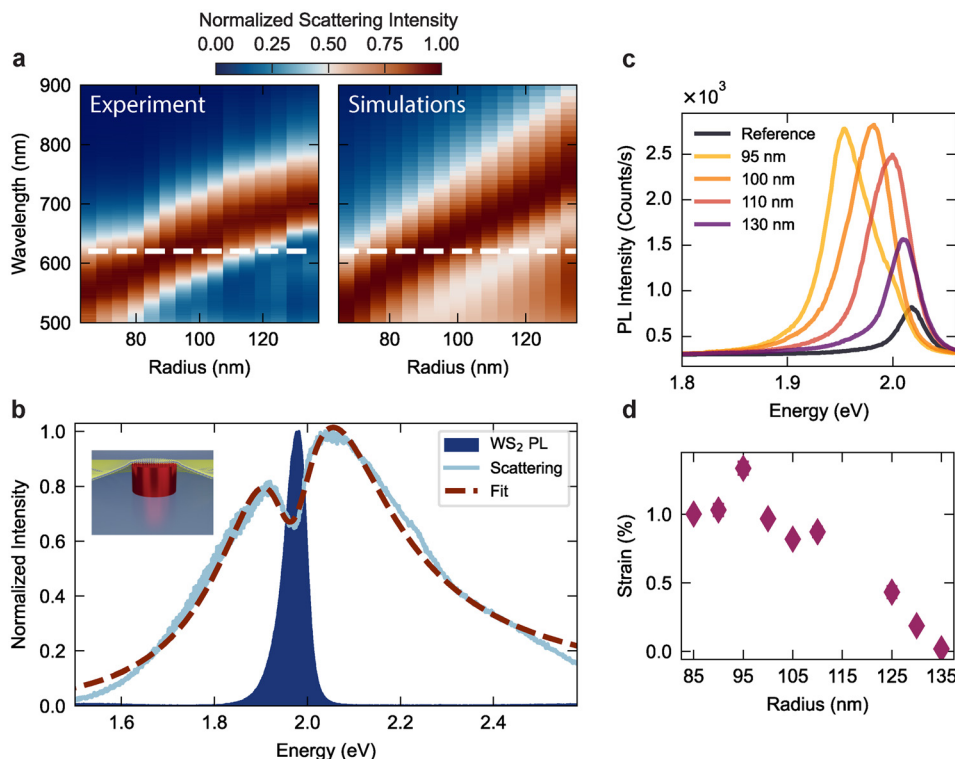
Fig. 2 (a) Experimental measurements (left) and numerical FDTD simulations (right) of the dark field scattering cross-section, presented as the normalized scattering intensity as a function of radius for GaP nanoantennas with fixed height 100 nm, on silica substrates. The resonance wavelength of WS$_2$ monolayer exciton emission is indicated by the dashed white line. (b) PL emission and dark field scattering spectra of a WS$_2$ monolayer coupled to a GaP nanoantenna with radius of 90 nm. The dashed line is a fit with the coupled oscillator model described in eqn (3) (see also ESI note 6†). Inset: Illustration of the WS$_2$ monolayer/GaP nanoantenna system. (c) PL spectra of monolayer WS$_2$ coupled to GaP nanoantennas with different radii, compared with the reference PL emission from WS$_2$ on a bare SiO$_2$ substrate. (d) Relative strain values extracted from the exciton peak position, using the empirical dependence of −50 meV/%.[39]

parison with numerical FDTD calculations for the same antenna geometry. The fabricated structures exhibit excellent agreement with the calculated results, with the predicted resonance redshift in larger structures. A maximal spectral overlap with the WS$_2$ exciton emission (dashed white line in Fig. 2a) is observed for a radius of approximately 90 nm. After transferring the WS$_2$ monolayer onto selected nanoantennas, we performed PL and dark field scattering spectroscopy. The reference darkfield scattering and PL spectra of a WS$_2$ monolayer on a GaP nanoantenna with radius of 90 nm are shown in Fig. 2b. Here, the scattering profile exhibits a noticeable dip at the WS$_2$ exciton resonance, arising from the resonant coupling between excitons and the spectrally broad Mie modes of the GaP nanoantenna. The interaction between the 2D excitons and the nanoantenna can be described by a COM in the form:[12,23]

$$\sigma_{scat}(\omega) = A\omega^4 \left| \frac{(\omega_X^2 - \omega^2 - i\omega\gamma)}{(\omega_{cav}^2 - \omega^2 - i\omega\kappa)(\omega_X^2 - \omega^2 - i\omega\gamma) - \omega_X\omega_{cav}g^2} \right|^2 \quad (3)$$

where $\sigma_{scat}(\omega)$ is the scattering cross-section and A is a scaling constant. Using this expression, we fit to the experimental

dark field scattering data (Fig. 2b) and extract a coupling constant of $g = 96 \pm 2$ meV (see also ESI Table 1†). Compared to the strong coupling condition of $|g| > \left| \frac{\kappa + \gamma}{4} \right| = 117.5$ meV, our system falls in an intermediate light–matter coupling regime prior to the introduction of the metallic mirror.[34]

We further extract the tensile strain present in our WS$_2$ layers as a function of the GaP resonator radius by analysis of the exciton spectral shifts in the PL profiles. Fig. 2c shows the PL emission spectra for WS$_2$ on GaP nanoantennas with different radii, showing increasing red shifts with reduced structure dimensions. The redshift of the PL peak can be translated into an effective strain value with the empirical relationship of −50 meV/%.[39] Fig. 2d shows the tensile strain values extracted from the PL spectra, reaching values of approximately 1%, with the expected increase for smaller nanostructures.[40] We note that, the magnitude of the shift for the maximum strain still lies well within the total width of the cavity scattering resonance, and inhomogeneities in the nanoscale strain profile induce a broadening of the exciton linewidths, directly affecting the coupling strength of each nanocavity.

For comprehensive comparison of changes in the PL spectral profile, we conducted spatially dependent PL measurements, where the diffraction-limited excitation laser spot was linearly scanned across the nanoantenna position. Fig. 3a shows the hyperspectral PL emission map for a WS$_2$ monolayer on a single GaP nanoantenna, collected by scanning the diffraction-limited 532 nm laser spot across the position of the antenna, centered at x = 0 nm. The PL signal was collected from the nanoantenna side, in a back reflection geometry, through the same excitation objective (NA = 0.9). From the spatial emission, we find that the co-localization of tensile strain and near-field enhancement at the nanoantenna position induces a substantial exciton red-shift[40] and a strong PL enhancement.[36] Fig. 3b shows the PL spectra, extracted from vertical profiles in Fig. 3a, for WS$_2$ coupled to the nanoantenna (x = 0 nm) and on the bare SiO$_2$ substrate (x = 250 nm). The coupled WS$_2$ spectrum exhibits a broadening, owing to inhomogeneous strain profiles in the deformed monolayer, along with the redshift due to tensile strain.

Following the characterization of the WS$_2$ on the isolated GaP nanoantenna, we incorporated the gold mirror to form a complete nanoparticle-on-mirror resonator. Fig. 3c and d presents the hyperspectral PL map of the same nanoantenna discussed above, but after the mirror integration. The PL signal is now collected from the SiO$_2$ substrate side. Compared to the previous case, we observe an overall increase in the relative PL intensity between excitons outside the cavity region and the nanocavity-coupled excitons, which can be ascribed to reflections of the mirror, leading to higher excitation and collection efficiency of PL emission from the uncoupled area. Importantly, at the nanoantenna position, the PL spectrum is characterized by a doublet, redshifted from the unstrained exciton and spatially localized within the nanogap (Fig. 3c). Fig. 3d shows a comparison of the spectral emission collected on and off the nanocavity. Both spectral contributions to the doublet appear at energies below the neutral exciton resonance. Considering the origin of the doublet from within the nanoparticle-on-mirror cavity, we note that no PL emission peak splitting is observed from antennas that are spectrally
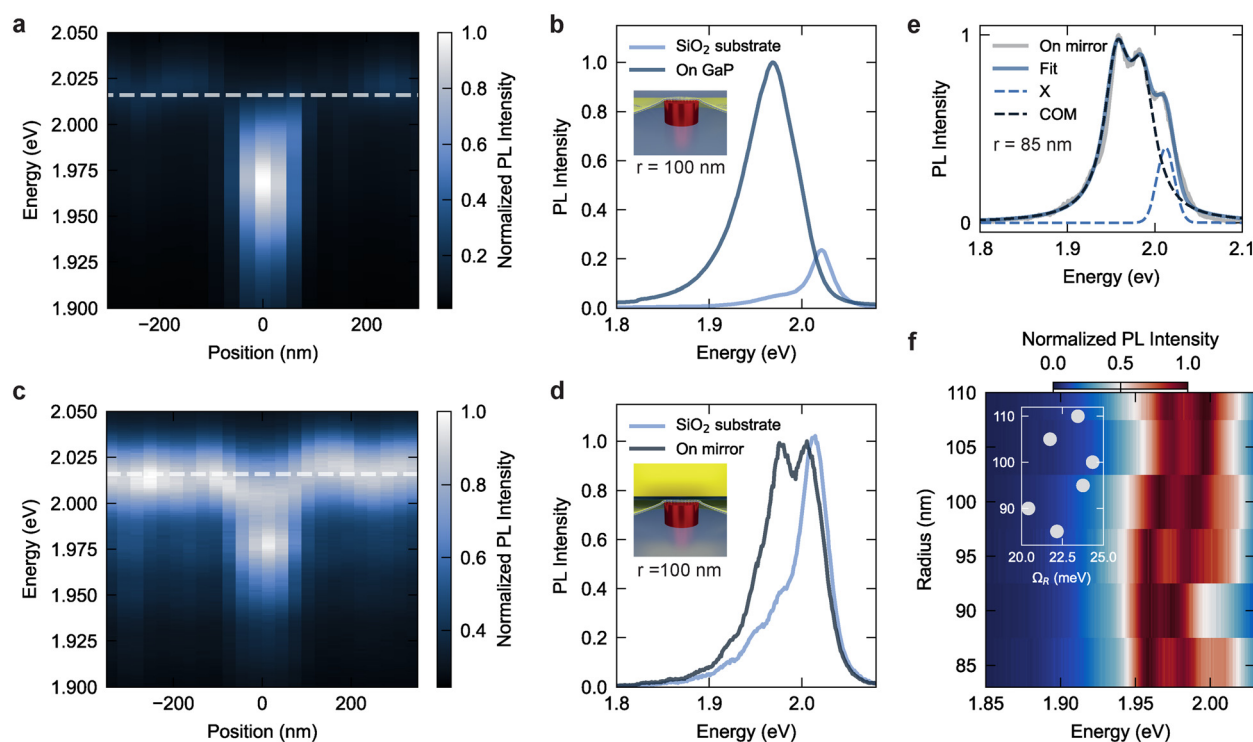
Fig. 3 (a) Room-temperature hyperspectral PL emission map for a WS$_2$ monolayer coupled to a GaP nanoantenna with 100 nm radius. The excitation laser is scanned linearly across the nanoantenna position, centered at x = 0 nm. (b) Comparison of PL spectra for the uncoupled exciton on a SiO$_2$ substrate to that from the exciton coupled to the GaP nanoantenna, with the latter exhibiting the expected strain-induced red shift and broadening. The spectra are normalized to the coupled emission intensity maximum. (c) WS$_2$ hyperspectral PL emission map from the same nanoantenna shown in (a) but with the presence of the gold mirror to generate the nanocavity gap. (d) PL spectrum for the uncoupled exciton on the SiO$_2$ substrate (at x = 250 nm) compared to the emission at the nanogap position (at x = 0), revealing characteristic splitting for the coupled exciton emission. The spectra are normalized to the coupled emission intensity maximum. (e) PL spectrum from monolayer WS$_2$ embedded in a hybrid nanocavity with GaP nanoantenna radius of 85 nm. The spectrum is fitted with a coupled oscillator model (COM) following eqn (4) (black dashed line), along with a Gaussian peak (blue dashed line) that accounts for the uncoupled and unstrained exciton emission peak (X) (see also ESI note 6†). (f) PL emission from monolayer WS$_2$ in hybrid nanocavities comprising GaP nanoantennas with radii from 85 to 110 nm. Inset: Rabi energy (Ω_R) values extracted with the COM model in eqn (4).
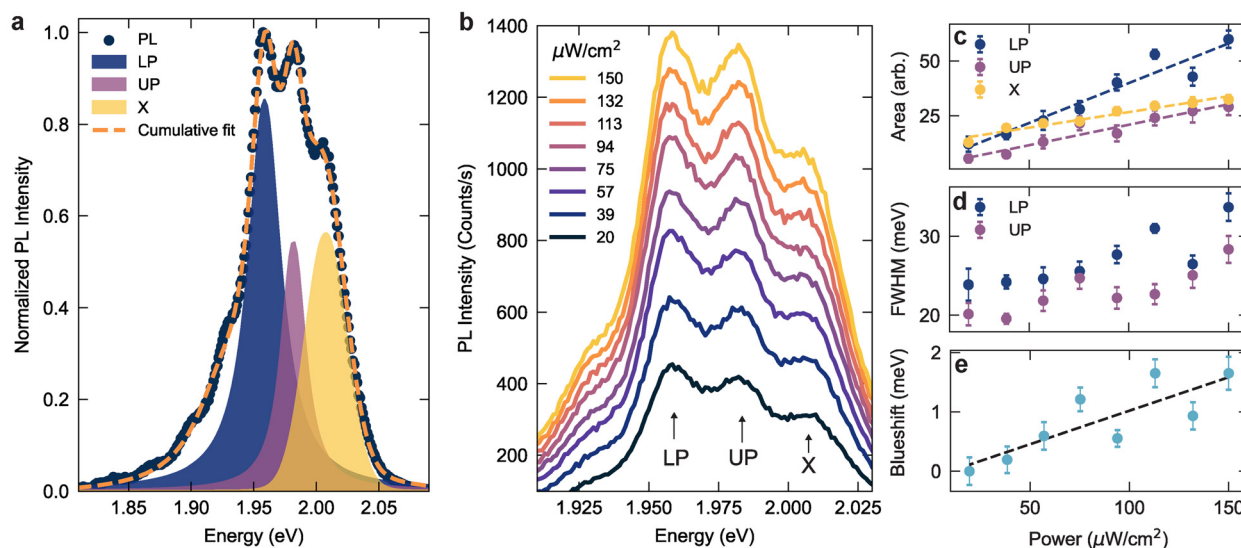
Fig. 4 (a) PL emission of monolayer WS_2 embedded in a hybrid nanocavity (GaP nanoantenna radius of 85 nm). The emission peaks are fitted with Voigt profiles. The uncoupled exciton (X) exhibits a Gaussian broadening, while the polariton branches are predominantly characterized by Lorentzian profiles. The dashed orange line is the cumulative fit. (b) Hybrid nanocavity-coupled WS_2 PL emission as a function of the excitation power. (c and d) Integrated peak area (c) and full width at half maximum (FWHM) (d) extracted from Voigt profile fits of the data in (b). (e) Blueshift of the PL dip, fitted with a Gaussian function. The dashed lines in (c and e) are linear fits to the respective data.

off-resonance from the WS_2 exciton (ESI Fig. S2a†). In addition, we detect a blueshift in the exciton resonance when introducing the mirror (see ESI Fig. S2b†), ascribed to changes in dielectric screening induced by the metallic surface. As the field confinement in the nanogap is found to be mainly independent of the radius of the investigated nanoantenna (see ESI note 3†), we consider the possibility that the lack of splitting in off-resonant cavities could be related to nanoscale variations in the distance between antenna and mirror, as well as inhomogeneous strain, both of which could vary with nanoantenna size and impact, for example, the formation of trions in the 2D semiconductor.[41] However, we can rule out dark excitons and trions as the origin of the PL peak splitting since these are usually observed at cryogenic temperatures, and at energies between 40 and 60 meV below the neutral exciton resonance,[32,42–46] larger than the splitting observed in our experiments (< 25 meV). Similarly, we can rule out defect states as these are commonly observed as a broad emission peak at lower energies.[47,48] We thus find that the PL emission doublet is a signature of polaritonic emission induced by the interaction between excitons located at the top of the nanoantenna and the confined optical field in the nanometer-sized gap between the nanoantenna and mirror. We further probed the scattering of the nanoparticle-on-mirror cavity, however, the signal exhibits pronounced fringes due to multiple reflections within the 150 µm thick coverslip above the particle-on-mirror cavity, hindering the evidence of strong coupling in the scattering spectra (see ESI note 4†). We note, however, that we observe larger splitting in the scattering spectra with values above 50 meV, twice than those observed in PL emission.

The PL intensity emitted by the exciton–polariton system, $I_X(\omega)$, can be modelled within a COM using the following formula:[23,25]

$$I_X(\omega) = A'\frac{\gamma}{2\pi}\left|\frac{\frac{\kappa}{2} - i(\omega - \omega_{cav})}{\left[\frac{\kappa + \gamma}{4} + \frac{i(\omega_{cav} - \omega_X)}{2} - i(\omega - \omega_X)\right]^2 + \Omega_R^2}\right|^2 \quad (4)$$

where A' is a scaling constant. Fig. 3e shows the PL spectrum of a WS_2 monolayer in a hybrid nanocavity for a nanoantenna with 85 nm radius. In this case, we observe the presence of both the uncoupled exciton resonance, at approximately 2.01 eV, and the redshifted doublet. To fit the complete spectrum, we use eqn (4) together with an additional Gaussian function describing the uncoupled exciton peak (dashed lines in Fig. 3e). This model provides a good fit to the experimental PL data and yields a coupling strength of 15.3 meV, comparable to the estimated strong coupling condition of approximately 15.0 meV, placing the system at the onset of the strong light–matter coupling regime. Moreover, from the fitted values, we extract κ values below 100 meV, indicating a reduction of the Mie resonance linewidths in GaP nanoantennas when the mirror is present, confirmed by numerical simulations shown in ESI Fig. S4.† Additionally, Fig. 3f shows the PL emission from different hybrid nano-cavities comprising GaP nanoantennas with radii between 85 nm and 110 nm. Here, the PL splitting is observed for all the resonant nanoantennas, redshifted from the neutral exciton resonance. The inset in Fig. 3f shows the values of the Rabi energies extracted from fitting the PL emission data with eqn (4), resulting in an average value of

22.6 meV. We note that nanoscale variations in the WS$_2$ morphology, together with the particle-mirror distance, directly influence the coupling strength in different cavities.

To further unveil the nature of the hybrid nanocavity PL emission, we investigated the individual contributions of the PL peak components as a function of excitation power. As shown in Fig. 3f, for several nanoantennas we observed a splitting in the PL emission of the redshifted strained exciton, along with an additional peak from the uncoupled exciton. Fig. 4a shows a fit of such a PL spectrum with three Voigt profiles (see also ESI note 5†), corresponding to the LP and UP peaks of the coupled excitons and, at higher energies, the emission of unstrained excitons (X). The redshifted polariton doublet in the PL spectrum is co-located with the strained area in the WS$_2$ monolayer and the gap formed with the metallic mirror. We note that deformations in the strained region could lead to a distribution of out-of-plane orientations of the excitonic dipoles, promoting an effective enhancement of the light–matter interaction and facilitating the coupling with 2D excitons.

Fig. 4b shows the PL emission spectra as a function of excitation power, from which we extracted the relative peak areas and linewidths, as well as Lorentzian and Gaussian weights. Fig. 4c shows the integrated area for each peak as a function of excitation power, which reveals a stronger linear dependence for the polaritonic branches compared to uncoupled excitons. Namely, the excitation power dependence of the emission intensity is 1.3 times larger for the UP peak and 2.5 times larger for the LP peak. From the Voigt profiles, we also extract an increase in linewidth and a predominant Lorentzian line shape at higher intensities for the polaritonic branches, as predicted from the more coherent PL emission of polaritonic states compared to bare excitons.[49] In ESI Fig. S6† we show the relative weights of the Gaussian and Lorentzian fits for each of the component peaks. At high excitation power, the polaritonic emission can be fitted with a Lorentzian function, while the neutral exciton exhibits a predominant Gaussian character, independent of the excitation power. Moreover, while UP emission is usually hindered in the PL emission, the small energy splitting comparable to thermal excitations, could promote recombination from the UP state even in the presence of relaxation processes. We further fitted the dip in the PL doublet with a Gaussian function[50] and plotted the extracted energy minima in Fig. 4e. This observed energy blueshift with increasing excitation power provides further support for the picture of strongly interacting exciton–polaritons, confined within the small nanocavity gap volume.

Conclusions

In summary, we investigated hybrid dielectric nanoparticle-on-mirror nanocavities, incorporating WS$_2$ monolayers between GaP Mie-resonant dielectric nanoantennas and a reflective gold mirror, to manipulate light–matter interactions in 2D semiconductors. Optical spectroscopy revealed an intermediate coupling regime of WS$_2$ coupled to single nanoantennas. After introducing the mirror, we observed a modal splitting in the PL signal of coupled excitons arising from the strong interaction between 2D confined excitons and the optical fields within the nanogap. Using a coupled harmonic oscillator model, we extracted Rabi splitting values ranging from 20 to 24 meV at room temperature. The origin of the splitting was confirmed by analysis of spatial and spectral PL emission data, which demonstrated a Lorentzian profile of the polaritonic peaks and a blueshift with increasing excitation power. These findings hold promise for the application of 2D hybrid nanophotonic structures for polaritonic devices at room temperature.[51] Moreover, the use of piezoelectric or phase change materials as dielectric resonators could provide a route to tailor the strain magnitude in the 2D materials, fixed in our approach during the transfer process. Our approach aimed to develop a top-down route for nanoparticle-on-mirror cavities, and while the current design is not yet suitable for practical applications, establishing a higher degree of control and stability by optimizing the contact between lithographically defined particles and the reflective mirror, for instance *via* micromanipulation,[52] as well as the use of monocrystalline metallic mirrors, could potentially provide enhanced control over light–matter interactions, towards the implementation of 2D single photon sources,[53] van der Waals heterostructures,[54] and Moiré superlattices[55] in hybrid nanophotonic platforms.

Author contributions

M. G. and B. T. fabricated the GaP samples. M. G. transferred the WS$_2$ monolayers. P. B. performed the ALD deposition. M. G., T. P., and L. S. carried out optical spectroscopic measurements. M. G. and L. S. analysed the data. L. d. S. M., I. D. S. and S. A. M. managed various aspects of the project. L. S. conceived the idea and supervised the project. The manuscript was written through the contributions of all authors. All authors have given approval to the final version of the manuscript.

Data availability

The data that support the findings of this study are available from **https://doi.org/10.5281/zenodo.13120851**.

Conflicts of interest

There are no conflicts to declare.

Acknowledgements

References

1 J. J. Baumberg, J. Aizpurua, M. H. Mikkelsen and D. R. Smith, *Nat. Mater.*, 2019, **18**, 668–678.

2 J. Jeong, H. W. Kim and D. S. Kim, *Nanophotonics*, 2022, **11**, 1231–1260.

3 Y. Yang, D. Zhu, W. Yan, A. Agarwal, M. Zheng, J. D. Joannopoulos, P. Lalanne, T. Christensen, K. K. Berggren and M. Soljačić, *Nature*, 2019, **576**, 248–252.

4 C. Ciracì, R. T. Hill, J. J. Mock, Y. Urzhumov, A. I. Fernández-Domínguez, S. A. Maier, J. B. Pendry, A. Chilkoti and D. R. Smith, *Science*, 2012, **337**, 1072–1074.

5 K. J. Savage, M. M. Hawkeye, R. Esteban, A. G. Borisov, J. Aizpurua and J. J. Baumberg, *Nature*, 2012, **491**, 574–577.

6 J. Sun, Y. Li, H. Hu, W. Chen, D. Zheng, S. Zhang and H. Xu, *Nanoscale*, 2021, **13**, 4408–4419.

7 G.-C. Li, Q. Zhang, S. A. Maier and D. Lei, *Nanophotonics*, 2018, **7**, 1865–1889.

8 A. Reserbat-Plantey, I. Epstein, I. Torre, A. T. Costa, P. A. D. Gonçalves, N. A. Mortensen, M. Polini, J. C. W. Song, N. M. R. Peres and F. H. L. Koppens, *ACS Photonics*, 2021, **8**, 85–101.

9 Y. Koo, T. Moon, M. Kang, H. Joo, C. Lee, H. Lee, V. Kravtsov and K.-D. Park, *Light: Sci. Appl.*, 2024, **13**, 30.

10 A. Krasnok, S. Lepeshov and A. Alú, *Opt. Express*, 2018, **26**, 15972.

11 Y. Meng, J. Feng, S. Han, Z. Xu, W. Mao, T. Zhang, J. S. Kim, I. Roh, Y. Zhao, D.-H. Kim, Y. Yang, J.-W. Lee, L. Yang, C.-W. Qiu and S.-H. Bae, *Nat. Rev. Mater.*, 2023, **8**, 498–517.

12 L. Huang, A. Krasnok, A. Alú, Y. Yu, D. Neshev and A. E. Miroshnichenko, *Rep. Prog. Phys.*, 2022, **85**, 046401.

13 G. Wang, A. Chernikov, M. M. Glazov, T. F. Heinz, X. Marie, T. Amand and B. Urbaszek, *Rev. Mod. Phys.*, 2018, **90**, 021001.

14 D. Zheng, S. Zhang, Q. Deng, M. Kang, P. Nordlander and H. Xu, *Nano Lett.*, 2017, **17**, 3809–3814.

15 J. Qin, Y. H. Chen, Z. Zhang, Y. Zhang, R. J. Blaikie, B. Ding and M. Qiu, *Phys. Rev. Lett.*, 2020, **124**, 63902.

16 J. Wen, H. Wang, W. Wang, Z. Deng, C. Zhuang, Y. Zhang, F. Liu, J. She, J. Chen, H. Chen, S. Deng and N. Xu, *Nano Lett.*, 2017, **17**, 4689–4697.

17 B.-Y. Wen, J.-Y. Wang, T.-L. Shen, Z.-W. Zhu, P.-C. Guan, J.-S. Lin, W. Peng, W.-W. Cai, H. Jin, Q.-C. Xu, Z.-L. Yang, Z.-Q. Tian and J.-F. Li, *Light: Sci. Appl.*, 2022, **11**, 235.

18 D. O. Sigle, J. Mertens, L. O. Herrmann, R. W. Bowman, S. Ithurria, B. Dubertret, Y. Shi, H. Y. Yang, C. Tserkezis, J. Aizpurua and J. J. Baumberg, *ACS Nano*, 2015, **9**, 825–830.

19 X. Liu, J. Yi, S. Yang, E.-C. Lin, Y.-J. Zhang, P. Zhang, J.-F. Li, Y. Wang, Y.-H. Lee, Z.-Q. Tian and X. Zhang, *Nat. Mater.*, 2021, **20**, 1210–1215.

20 C. Li, X. Lu, A. Srivastava, S. D. Storm, R. Gelfand, M. Pelton, M. Sukharev and H. Harutyunyan, *Nano Lett.*, 2021, **21**, 1599–1605.

21 Y. Luo, G. D. Shepard, J. V. Ardelean, D. A. Rhodes, B. Kim, K. Barmak, J. C. Hone and S. Strauf, *Nat. Nanotechnol.*, 2018, **13**, 1137–1142.

22 X. Xu, A. B. Solanki, D. Sychev, X. Gao, S. Peana, A. S. Baburin, K. Pagadala, Z. O. Martin, S. N. Chowdhury, Y. P. Chen, T. Taniguchi, K. Watanabe, I. A. Rodionov, A. V. Kildishev, T. Li, P. Upadhyaya, A. Boltasseva and V. M. Shalaev, *Nano Lett.*, 2023, **23**, 25–33.

23 M. Pelton, S. D. Storm and H. Leng, *Nanoscale*, 2019, **11**, 14540–14552.

24 M. Wersäll, J. Cuadra, T. J. Antosiewicz, S. Balci and T. Shegai, *Nano Lett.*, 2017, **17**, 551–558.

25 K.-D. Park, M. A. May, H. Leng, J. Wang, J. A. Kropp, T. Gougousi, M. Pelton and M. B. Raschke, *Sci. Adv.*, 2019, **5**, 1–8.

26 J. Sun, H. Hu, D. Zheng, D. Zhang, Q. Deng, S. Zhang and H. Xu, *ACS Nano*, 2018, **12**, 10393–10402.

27 M. Caldarola, P. Albella, E. Cortés, M. Rahmani, T. Roschuk, G. Grinblat, R. F. Oulton, A. V. Bragas and S. A. Maier, *Nat. Commun.*, 2015, **6**, 7915.

28 S. Shen, Y. Wu, Y. Li, P. Xie, Q. Ding, X. Kuang, W. Wang and W. Wang, *Phys. Rev. B*, 2022, **105**, 155403.

29 K. As'ham, I. Al-Ani, M. Alaloul, S. Abdo, A. Abdulghani, W. Lei, H. T. Hattori, L. Huang and A. E. Miroshnichenko, *Phys. Rev. Appl.*, 2023, **19**, 054049.

30 H. Sugimoto and M. Fujii, *ACS Photonics*, 2018, **5**, 1986–1993.

31 F. Deng, H. Huang, J.-D. Chen, S. Liu, H. Pang, X. He and S. Lan, *Nano Lett.*, 2022, **22**, 220–228.

32 S. Liu, F. Deng, W. Zhuang, X. He, H. Huang, J.-D. Chen, H. Pang and S. Lan, *ACS Nano*, 2022, **16**, 14390–14401.

33 J. Fang, K. Yao, M. Wang, Z. Yu, T. Zhang, T. Jiang, S. Huang, B. A. Korgel, M. Terrones, A. Alù and Y. Zheng, *Nano Lett.*, 2023, **23**, 9803–9810.

34 L. Sortino, M. Gülmüs, B. Tilmann, L. de S. Menezes and S. A. Maier, *Light: Sci. Appl.*, 2023, **12**, 202.

35 M.-E. Kleemann, R. Chikkaraddy, E. M. Alexeev, D. Kos, C. Carnegie, W. Deacon, A. C. de Pury, C. Große, B. de Nijs, J. Mertens, A. I. Tartakovskii and J. J. Baumberg, *Nat. Commun.*, 2017, **8**, 1296.

36 L. Sortino, P. G. Zotev, S. Mignuzzi, J. Cambiaso, D. Schmidt, A. Genco, M. Aßmann, M. Bayer, S. A. Maier, R. Sapienza and A. I. Tartakovskii, *Nat. Commun.*, 2019, **10**, 5119.

37 T. Bucher, A. Vaskin, R. Mupparapu, F. J. F. Löchner, A. George, K. E. Chong, S. Fasold, C. Neumann, D.-Y. Choi, F. Eilenberger, F. Setzpfandt, Y. S. Kivshar, T. Pertsch,

A. Turchanin and I. Staude, *ACS Photonics*, 2019, **6**, 1002–1009.

38 Y. Liu, N. O. Weiss, X. Duan, H.-C. Cheng, Y. Huang and X. Duan, *Nat. Rev. Mater.*, 2016, **1**, 16042.

39 I. Niehues, R. Schmidt, M. Drüppel, P. Marauhn, D. Christiansen, M. Selig, G. Berghäuser, D. Wigger, R. Schneider, L. Braasch, R. Koch, A. Castellanos-Gomez, T. Kuhn, A. Knorr, E. Malic, M. Rohlfing, S. Michaelis de Vasconcellos and R. Bratschitsch, *Nano Lett.*, 2018, **18**, 1751–1757.

40 L. Sortino, M. Brooks, P. G. Zotev, A. Genco, J. Cambiasso, S. Mignuzzi, S. A. Maier, G. Burkard, R. Sapienza and A. I. Tartakovskii, *ACS Photonics*, 2020, **7**, 2413–2422.

41 M. G. Harats, J. N. Kirchhof, M. Qiao, K. Greben and K. I. Bolotin, *Nat. Photonics*, 2019, **14**, 324–329.

42 J. Shi, J. Zhu, X. Wu, B. Zheng, J. Chen, X. Sui, S. Zhang, J. Shi, W. Du, Y. Zhong, Q. Wang, Q. Zhang, A. Pan and X. Liu, *Adv. Opt. Mater.*, 2020, **8**, 1–9.

43 Z. Wang, Y. Liu, D. Chen, Z. Wang, M. Asbahi, S. D. Rezaei, J. Deng, J. Teng, A. T. S. Wee, W. Zhang, J. K. W. Yang and Z. Dong, *Sci. Rep.*, 2022, **12**, 15861.

44 N. S. Mueller, R. Arul, G. Kang, A. P. Saunders, A. C. Johnson, A. Sánchez-Iglesias, S. Hu, L. A. Jakob, J. Bar-David, B. de Nijs, L. M. Liz-Marzán, F. Liu and J. J. Baumberg, *Nat. Commun.*, 2023, **14**, 5726.

45 K.-D. Park, T. Jiang, G. Clark, X. Xu and M. B. Raschke, *Nat. Nanotechnol.*, 2018, **13**, 59–64.

46 T. W. Lo, X. Chen, Z. Zhang, Q. Zhang, C. W. Leung, A. V. Zayats and D. Lei, *Nano Lett.*, 2022, **22**, 1915–1921.

47 P. K. Chow, R. B. Jacobs-Gedrim, J. Gao, T.-M. Lu, B. Yu, H. Terrones and N. Koratkar, *ACS Nano*, 2015, **9**, 1520–1527.

48 Z. Wu, W. Zhao, J. Jiang, T. Zheng, Y. You, J. Lu and Z. Ni, *J. Phys. Chem. C*, 2017, **121**, 12294–12299.

49 F. P. Laussy, E. del Valle and C. Tejedor, *Phys. Rev. B: Condens. Matter Mater. Phys.*, 2009, **79**, 1–17.

50 E. Maggiolini, L. Polimeno, F. Todisco, A. Di Renzo, B. Han, M. De Giorgi, V. Ardizzone, C. Schneider, R. Mastria, A. Cannavale, M. Pugliese, L. De Marco, A. Rizzo, V. Maiorano, G. Gigli, D. Gerace, D. Sanvitto and D. Ballarini, *Nat. Mater.*, 2023, **22**, 964–969.

51 D. Sanvitto and S. Kéna-Cohen, *Nat. Mater.*, 2016, **15**, 1061–1073.

52 P. G. Zotev, Y. Wang, D. Andres-Penares, T. Severs-Millard, S. Randerson, X. Hu, L. Sortino, C. Louca, M. Brotons-Gisbert, T. Huq, S. Vezzoli, R. Sapienza, T. F. Krauss, B. D. Gerardot and A. I. Tartakovskii, *Laser Photonics Rev.*, 2023, **17**(8), 2200957.

53 L. Sortino, P. G. Zotev, C. L. Phillips, A. J. Brash, J. Cambiasso, E. Marensi, A. M. Fox, S. A. Maier, R. Sapienza and A. I. Tartakovskii, *Nat. Commun.*, 2021, **12**, 6063.

54 M. Kremser, M. Brotons-Gisbert, J. Knörzer, J. Gückelhorn, M. Meyer, M. Barbone, A. V. Stier, B. D. Gerardot, K. Müller and J. J. Finley, *npj 2D Mater. Appl.*, 2020, **4**, 8.

55 L. Du, M. R. Molas, Z. Huang, G. Zhang, F. Wang and Z. Sun, *Science*, 2023, **379**, eadg0014.